Dalton Transactions

ROYAL SOCIETY OF CHEMISTRY

PAPER

View Article Online
View Journal | View Issue

Cite this: *Dalton Trans.*, 2026, **55**, 183

Methylated regioisomers of Re(I) and Ir(III) tetrazole complexes: photophysical properties and optical imaging of brain tissue

Elena Dallerba, [a] Lee J. Cameron, [a] Blake I. Armstrong, [a] Gaewyn Ellison, [a] Eva Turner,[a] Evelyn S. Innes, [a] Georgia L. Strickling,[a] Joel Pangiarella, [a] Peter Ó. Conghaile,[b] Michael Nesbit,[c] Stephen A. Moggach, [d] Paolo Raiteri, [a] Stefano Stagni, [e] Emma L. Pearson,[a] Mark J. Hackett *[a,c] and Massimiliano Massi *[a]

Coordination of *N*1 and *N*2-methylated regioisomers of 2-(1*H*-tetrazol-5-yl)pyridine and 2-(1*H*-tetrazol-5-yl)quinoline to $ReBr(CO)_3$ and $Ir(\mathbf{ppy})_2^+$ (**ppy** = cyclometalated 2-phenylpyridine) fragments resulted in the isolation of a small family of Re(I) and Ir(III) luminescent complexes. The complexes display phosphorescent emission from their triplet ligand-to-metal charge transfer excited states in degassed solution at room temperature. Notably, the position of the methyl substituent has a profound effect on the photophysical properties. The *N*1-methylated complexes in all cases display a significant redshift in the emission band. The shift is ascribed to a stabilisation of the π^* orbitals of the tetrazole ligands, which is also supported by cyclic voltammetry and time-dependent density functional theory (TD-DFT) calculations. The complexes were used as luminescent labels for the staining of mouse brain tissue. The Re(I) complexes did not show any evident staining. On the other hand, the Ir(III) complexes – particularly those bound to the ligand containing the quinoline substituent – demonstrated affinity for lipid-rich myelinated regions in brain tissues and white matter in cerebellum tissues. The specificity of the Ir(III) complexes was further demonstrated by means of correlative optical microscopy and Fourier transform infrared (FTIR) microscopy.

Received 24th July 2025,
Accepted 4th November 2025

DOI: 10.1039/d5dt01745a

rsc.li/dalton

Introduction

Imaging techniques such as fluorescent microscopy play a pivotal role in elucidating the cellular architecture and molecular landscape of the brain.[1] By employing fluorescent probes that selectively target specific biological components, this method enables detailed investigation of cellular morphology, dynamic processes, and chemical composition within neural tissues.[2,3] To investigate disease mechanisms or elucidate the biochemical mode of action of novel therapeutics, relevant *in vitro* cell culture or animal models can be employed. Unfortunately, the complex interactions of molecular pathways within tissue physiology are often not well modelled *in vitro*, with most fluorescence probes developed for and validated in cell culture being incompatible with animal tissues.[3] In this context, *ex vivo* brain tissue analysis is an emerging tool that can provide high-resolution insight into probe distribution, target engagement, and localised biochemical changes within defined brain regions. Most probes for optical imaging are based around organic fluorophores.[4] However, depending on the imaging conditions, these can suffer from common drawbacks such as photobleaching, concentration quenching and interference from autofluorescence.[5–7]

In the last few decades, luminescent transition metal complexes have emerged as versatile platforms for optical imaging, amongst other fields such as optoelectronic devices, sensing and photocatalysis.[8–10] Transition metals with low-spin d^6 electronic configuration – like Ru(II), Re(I) and Ir(III) – or d^8 electronic configuration – like Pt(II) and Au(I) – have been extensively investigated.[11,12] Typically, these complexes are luminescent due to phosphorescent emission from their triplet metal-to-ligand charge transfer (^{3}MLCT) excited states,

[a]*School of Molecular and Life Sciences, Curtin University, Perth, WA, Australia. E-mail: mark.j.hackett@curtin.edu.au, m.massi@curtin.edu.au*
[b]*School of Electrical Engineering, Computing and Mathematical Sciences, Curtin University, Perth, WA, Australia*
[c]*Curtin Health Innovation Research Centre and School of Population Health, Curtin University, Perth, WA, Australia*
[d]*School of Molecular Sciences, The University of Western Australia, Perth, WA, Australia*
[e]*Department of Industrial Chemistry "Toso Montanari", University of Bologna, Bologna, Italy*

whose population is facilitated by the strong spin–orbit coupling of the metal centre *via* intersystem crossing from singlet excited states. Their photophysical properties are versatile and can be manipulated by varying the chemical structure of the coordinated ligands. In a similar manner, ligand variation provides a means to alter the biological behaviour of the complex in terms of cytotoxicity, permeation through membranes, association with specific cellular substrates and localisation within targeted organelles.[11,13] Metal-based probes offer alternative chemical scaffolds that potentially alleviate the above-mentioned drawbacks of organic fluorophores, due to their phosphorescent nature characterised by large Stoke shifts and relatively long excited-state lifetimes.[14] It should be noted that, while luminescent transition metal complexes have been extensively investigated as probes for *ex vivo* optical imaging, this effort has predominantly been focused on the imaging of fixed and/or live cellular substrates. On the other hand, imaging of tissue stained with luminescent metal complexes has comparatively received less attention.[3] Nonetheless, it is quite evident that metal-based probes offer significant benefit in the field of tissue staining. Therefore, there is a need to develop optimised staining procedures and diagnostic protocols for the imaging of tissue samples incubated with luminescent metal complexes.

In our previous studies, we have investigated tetrazolato complexes of Re(I)[15] and Ir(III)[16] as potential optical labels for the staining of both cells and tissue, in an effort to establish a structure–activity relationship linking the chemical nature of the ligands with the cellular behaviour of the complex. Methylation of the tetrazolato ligand has proven to be a facile and effective strategy for modulating the photophysical and biophysical properties of the complex.[17] This modification alters the relative energy of the ^{3}MLCT excited state and affects organelle targeting.[16] For example, methylation of the complex [Ir(**ppy**)$_2$**L**] (where **ppy** is a cyclometalated 2-phenylpyridine and **L** is a deprotonated 1*H*-5-(2′-yl-5′-(4″-cyanophenyl)-pyridine)-tetrazole) results in a redshift of the emission band and change in cellular localisation from the endoplasmic reticulum and lipid droplets towards mitochondria.[16] However, it appeared evident that cationic iridium complexes bound to methylated tetrazole ligands display more acute cytotoxicity when compared to neutral iridium complexes bound to anionic tetrazolato ligands. The change in biological properties is also retained for tissue staining, with the advantage that this cationic methylated complex is capable of staining mitochondria in preserved tissue and in the absence of the mitochondrial membrane potential.[18] Methylation of the tetrazolato complexes was performed directly on the coordinated tetrazolato ligand, forming exclusively the *N*2-methylated regioisomer.[17] The selectivity is presumably due to steric hindrance, reducing the nucleophilicity of the N1 atom. However, Bryce *et al.* have previously reported the preparation of luminescent Cu(I) complexes bound to *N*1 and *N*2-methylated 5-(2′-pyridyl)tetrazole ligands.[19] In their work, methylation of the free ligand yields a mixture of *N*1 and *N*2 regioisomers, which can be separated by means of column chromatography before complexation.

Following from the work of Bryce *et al.*, we wanted to investigate whether the preparation of *N*1 and *N*2-methylated regioisomers of Re(I) and Ir(III) complexes would provide a convenient strategy to obtain chemical structures as similar as possible in terms of charge and composition, but displaying modulation of their photophysical properties. The rationale behind this investigation is to access metal-based probes that have potentially the same biological target but different photophysical properties. This aspect would be advantageous since some experiments require staining with multiple probes that must display emission in different spectral regions to be independently imaged. As metal scaffolds, we have decided to use the $ReBr(CO)_3$ and $Ir(\mathbf{ppy})_2^+$ fragments and bind them to the *N*1 and *N*2-methylated regioisomers of 2-(1*H*-tetrazol-5-yl)pyridine (**P1** and **P2**) and 2-(2*H*-tetrazol-5-yl)quinoline (**Q1** and **Q2**). Brain tissue staining with the prepared complexes indicates that the Ir(III)-based probes might offer a promising building block for the design of imaging agents for the white matter. However, it was not possible to image samples stained with the Re(I)-based probes.

Experimental section

All reagents and solvents were purchased from Sigma Aldrich and used as received without further purification. 2-(1*H*-Tetrazol-5-yl)pyridine, 2-(1*H*-tetrazol-5-yl)quinoline and [Ir(ppy)$_2$(μ-Cl)]$_2$ were prepared according to previously reported methods.[16] ^{1}H, ^{13}C, H–H COSY and H–C HSQC nuclear magnetic resonance spectra were recorded using a Bruker Avance 400 spectrometer (400.1 MHz for ^{1}H, 100 MHz for ^{13}C) at room temperature. All NMR spectra are shown in Fig. S1–S45. Chemical shifts were referenced to residual solvent signals. Infrared spectra were recorded in the solid state, using an attenuated total reflectance PerkinElmer Spectrum 100 FT-IR, equipped with a diamond stage. Compounds were scanned from 4000 to 650 cm^{-1}. The intensities of the IR bands are reported as strong (s), medium (m), or weak (w). Elemental analyses were obtained using the facilities at the School of Molecular and Life Sciences at Curtin University. High Resolution Mass Spectroscopy (HRMS) data were collected at the University of Western Australia in electrospray positive ion (ESI+) mode.

Synthetic details

Warning! Azides and tetrazoles are potentially explosive compounds and should be handled with care. While no issues were encountered in the preparation of the reported species, it is advisable that reactions are carried out using relatively small scales.

Synthesis of methylated tetrazoles

The corresponding tetrazole (1.0 eq.), potassium carbonate (1.5 eq.) and iodomethane (1.1 eq.) were added to acetone (*ca.* 10 mL), and the resulting mixture was heated to 100 °C in a sealed pressure flask for 24 hours. After this time, undissolved

solids were filtered, and the solvent was removed under reduced pressure. The obtained solids were purified *via* flash chromatography, using silica as the stationary phase and a mixture of hexanes and ethyl acetate as eluent (7 : 3 and 4 : 1 for the pyridine and quinoline substrates, respectively).

2-(1-Methyl-1*H*-tetrazol-5-yl)pyridine (P1). Yield: 0.12 g (34%). ^{1}H NMR (DMSO-d_6, δ, ppm): 8.82 (d, J = 4.8 Hz, 1H, $\mathbf{H_6}$), 8.24 (d, J = 7.9 Hz, 1H, $\mathbf{H_3}$), 8.10 (app. t, J = 7.8 Hz, 1H, $\mathbf{H_4}$), 7.65 (app. t, J = 7.7 Hz, 1H, $\mathbf{H_5}$), 4.42 (s, 3H, $\mathbf{H_{Me}}$). ^{13}C NMR (DMSO-d_6, δ, ppm): 152.0 ($\mathbf{C_T}$), 149.8 ($\mathbf{C_6}$), 144.3 ($\mathbf{C_2}$), 138.2 ($\mathbf{C_4}$), 125.8 ($\mathbf{C_5}$), 124.2 ($\mathbf{C_3}$), 36.6 ($\mathbf{C_{Me}}$).

2-(2-Methyl-2*H*-tetrazol-5-yl)pyridine (P2). Yield: 0.09 g (25%). ^{1}H NMR (DMSO-d_6, δ, ppm): 8.75 (d, J = 4.8 Hz, 1H, $\mathbf{H_6}$), 8.13 (d, J = 7.9 Hz, 1H, $\mathbf{H_3}$), 8.01 (app. t, J = 7.7 Hz, 1H, $\mathbf{H_4}$), 7.55 (app. t, J = 7.6 Hz, 1H, $\mathbf{H_5}$), 4.46 (s, 3H, $\mathbf{H_{Me}}$). ^{13}C NMR (DMSO-d_6, δ, ppm): 164.1 ($\mathbf{C_T}$), 150.2 ($\mathbf{C_6}$), 146.3 ($\mathbf{C_2}$), 137.6 ($\mathbf{C_4}$), 125.2 ($\mathbf{C_5}$), 122.3 ($\mathbf{C_3}$). The CH_3 peak in the ^{13}C NMR spectrum overlaps with the solvent peak.

2-(1-Methyl-1*H*-tetrazol-5-yl)quinoline (Q1). Yield: 0.61 g (30%). ^{1}H NMR (DMSO-d_6, δ, ppm): 8.67 (d, J = 8.6 Hz, 1H, $\mathbf{H_3}$), 8.34 (d, J = 8.5 Hz, 1H, $\mathbf{H_4}$), 8.20 (d, J = 8.5 Hz, 1H, $\mathbf{H_9}$), 8.13 (d, J = 8.1 Hz, 1H, $\mathbf{H_6}$), 7.92 (app. t, J = 8.4 Hz, 1H, $\mathbf{H_8}$), 7.77 (app. t, J = 8.1 Hz, 1H, $\mathbf{H_7}$), 4.59 (s, 3H, $\mathbf{H_{Me}}$). ^{13}C NMR (DMSO-d_6, δ, ppm): 151.9 ($\mathbf{C_T}$), 146.7 ($\mathbf{C_{quat}}$), 144.6 ($\mathbf{C_{quat}}$), 138.2 ($\mathbf{C_3}$), 130.9 ($\mathbf{C_8}$), 129.3 ($\mathbf{C_9}$), 128.4 ($\mathbf{C_7}$), 128.2 ($\mathbf{C_6}$), 127.8 ($\mathbf{C_{quat}}$), 120.7 ($\mathbf{C_4}$), 37.0 ($\mathbf{C_{Me}}$).

2-(2-Methyl-2*H*-tetrazol-5-yl)quinoline (Q2). Yield: 0.29 g (14%). ^{1}H NMR (DMSO-d_6, δ, ppm): 8.60 (d, J = 8.6 Hz, 1H, $\mathbf{H_3}$), 8.27 (d, J = 8.5 Hz, 1H, $\mathbf{H_4}$), 8.15 (d, J = 8.5 Hz, 1H, $\mathbf{H_9}$), 8.09 (d, J = 8.1 Hz, 1H, $\mathbf{H_6}$), 7.87 (app. t, J = 8.4 Hz, 1H, $\mathbf{H_8}$), 7.71 (app. t, J = 8.1 Hz, 1H, $\mathbf{H_7}$), 4.51 (s, 3H, $\mathbf{H_{Me}}$). ^{13}C NMR (DMSO-d_6, δ, ppm): 164.2 ($\mathbf{C_T}$), 147.5 ($\mathbf{C_{quat}}$), 146.4 ($\mathbf{C_{quat}}$), 137.8 ($\mathbf{C_3}$), 130.6 ($\mathbf{C_8}$), 129.3 ($\mathbf{C_9}$), 128.1 ($\mathbf{C_7}$), 128.0 ($\mathbf{C_6}$), 127.7 ($\mathbf{C_{quat}}$), 119.6 ($\mathbf{C_4}$). The CH_3 peak in the ^{13}C NMR spectrum overlaps with the solvent peak.

Synthesis of rhenium complexes

$[ReBr(CO)_5]$ (1.0 eq.) and the corresponding methylated tetrazole (1.0 eq.) were combined in toluene (*ca.* 5.0 mL) and heated at reflux for 24 hours. The resulting yellow precipitate was vacuum filtered, then washed with toluene and diethyl ether to yield the targeted complex.

***fac*-[ReBr(CO)$_3$P1] (ReP1).** Yield: 0.15 g (88%). ^{1}H NMR (DMSO-d_6, δ, ppm): 9.18 (d, J = 5.5, Hz, 1H, $\mathbf{H_6}$), 8.60 (d, J = 8.1 Hz, 1H, $\mathbf{H_3}$), 8.45 (app. t, J = 7.9 Hz, 1H, $\mathbf{H_4}$), 7.92 (app. t, J = 7.8 Hz, 1H, $\mathbf{H_5}$), 4.61 (s, 3H, $\mathbf{H_{Me}}$). ^{13}C NMR (DMSO-d_6, δ, ppm): 196.7 (CO), 195.9 (CO), 187.9 (CO), 156.2 ($\mathbf{C_T}$), 154.8 ($\mathbf{C_6}$), 141.7 ($\mathbf{C_2}$), 140.8 ($\mathbf{C_4}$), 129.7 ($\mathbf{C_5}$), 126.6 ($\mathbf{C_3}$), 37.5 ($\mathbf{C_{Me}}$). IR-ATR (cm^{-1}): 2030 (CO), 1953 (CO), 1876 (CO). Anal. calcd for $C_{10}H_7N_5O_3BrRe$: C 23.49, H 1.38, N 13.70. Found: C 23.72, H 1.07, N 13.51. HRMS (m/z) calcd for $C_{10}H_7O_3N_5{}^{187}Re$ $[M\{-Br^-\}]^+$: 432.0106. Found: 432.0096. Calcd for $C_{12}H_{10}O_3N_{65}{}^{187}Re$ $[M\{-Br^-\} + ACN]^+$: 473.0372. Found: 473.0361. Single crystals for X-ray diffraction were grown from a slowly evaporating acetone/water solution.

***fac*-[ReBr(CO)$_3$P2] (ReP2).** Yield: 0.05 g (40%). ^{1}H NMR (DMSO-d_6, δ, ppm): 9.12 (d, J = 5.4 Hz, 1H, $\mathbf{H_6}$), 8.49 (d, J = 7.8 Hz, 1H, $\mathbf{H_3}$), 8.40 (app. t, J = 7.8 Hz, 1H, $\mathbf{H_4}$), 7.87 (app. t, J = 7.8 Hz, 1H, $\mathbf{H_5}$), 4.67 (s, 3H, $\mathbf{H_{PMe}}$). ^{13}C NMR (DMSO-d_6, δ, ppm): 196.4 (CO), 195.6 (CO), 188.0 (CO), 165.9 ($\mathbf{C_T}$), 154.4 ($\mathbf{C_6}$), 143.7 ($\mathbf{C_2}$), 141.4 ($\mathbf{C_4}$), 129.3 ($\mathbf{C_5}$), 124.3 ($\mathbf{C_3}$), 42.0 ($\mathbf{C_{Me}}$). IR-ATR (cm^{-1}): 2024 (CO), 1893 (CO), 1874 (CO). Anal. calcd for $C_{10}H_7N_5O_3BrRe$: C 23.49, H 1.38, N 13.70. Found: C 23.22, H 0.94, N 13.40. HRMS (m/z) calcd for $C_{10}H_7O_3N_5{}^{187}Re$ $[M\{-Br^-\}]^+$: 432.0106. Found: 432.0098. Calcd for $C_{12}H_{10}O_3N_{65}{}^{187}Re$ $[M\{-Br^-\} + ACN]^+$: 473.0372. Found 473.0363. Single crystals for X-ray diffraction were grown from a slowly evaporating acetone/water solution.

***fac*-[ReBr(CO)$_3$Q1] (ReQ1).** Yield: 0.02 g (86%). ^{1}H NMR (DMSO-d_6, δ, ppm): 9.11 (d, 1H, $\mathbf{H_3}$), 8.73 (d, J = 8.9, 1.0 Hz, 1H, $\mathbf{H_9}$), 8.66 (d, J = 8.6 Hz, 1H, $\mathbf{H_4}$), 8.40 (d, J = 8.2, 1.5 Hz, 1H, $\mathbf{H_6}$), 8.26 (app. t, J = 8.7 Hz, 1H, $\mathbf{H_8}$), 8.02 (app. t, J = 8.1 Hz, 1H, $\mathbf{H_7}$), 4.73 (s, 3H, $\mathbf{H_{Me}}$). The ^{13}C-NMR spectrum displayed duplication of peaks at higher concentration, which might be ascribed to the lower solubility of the complex. IR-ATR (cm^{-1}): 2023 (CO), 1923 (CO), 1892 (CO). Anal. calcd for $C_{14}H_9N_5O_3BrRe$: C 29.95, H 1.62, N: 12.48. Found: C 30.32, H 1.32, N 12.28. HRMS (m/z) calcd for $C_{16}H_{12}O_3N_6{}^{187}Re$ $[M\{-Br^-\} + ACN]^+$: 523.0528. Found: 523.0520. Single crystals for X-ray diffraction were grown from a slowly evaporating acetonitrile solution.

***fac*-[ReBr(CO)$_3$Q2] (ReQ2).** Yield: 0.06 g (74%). ^{1}H NMR (DMSO-d_6, *d*, ppm): 9.06 (d, J = 8.4 Hz, 1H, $\mathbf{H_3}$), 8.68 (d, J = 8.9 Hz, 1H, $\mathbf{H_9}$), 8.54 (d, J = 8.4 Hz, 1H, $\mathbf{H_4}$), 8.40–8.34 (m, 1H, $\mathbf{H_6}$), 8.23 (app. t, J = 8.6 Hz, 1H, $\mathbf{H_8}$), 7.98 (t, J = 7.5 Hz, 1H, $\mathbf{H_7}$), 4.74 (s, 3H, $\mathbf{H_{Me}}$). The ^{13}C-NMR spectrum displayed duplication of peaks at higher concentration, which might be ascribed to the lower solubility of the complex. IR-ATR (cm^{-1}): 2026 (CO), 1929 (CO), 1888 (CO). Anal. calcd for $C_{14}H_9N_5O_3BrRe$: C 29.95, H 1.62, N 12.48. Found: C 29.94, H 1.24, N 12.03. HRMS (m/z) calcd for $C_{16}H_{12}O_3N_6{}^{187}Re$ $[M\{-Br^-\} + ACN]^+$: 523.0528. Found: 523.0522. Single crystals for X-ray diffraction were grown by vapor diffusion of diethyl ether into a dichloromethane solution.

Synthesis of iridium complexes

$[Ir(\mathbf{ppy})_2(\mu\text{-}Cl)]_2$ (1 eq.) and the corresponding methylated tetrazole ligand (2.5 eq.) were combined in a 3 : 1 dichloromethane/ethanol mixture and stirred at room temperature for 24 hours. The solvents were removed under reduced pressure and the residual solid was dissolved in a minimal amount of methanol. A saturated aqueous KPF_6 solution was then added to cause the formation of a solid. The precipitate was collected *via* vacuum filtration, washed with water, and allowed to dry in air to yield the targeted complex.

[Ir(ppy)$_2$P1]PF$_6$ (IrP1). Yield: 0.05 g (44%). ^{1}H NMR (acetone-d_6, δ, ppm): 8.86 (d, J = 8.0 Hz, 1H), 8.44 (app. t, J = 7.9 Hz, 1H), 8.26–8.15 (m, 3H), 7.99–7.93 (m, 3H), 7.90–7.85 (m, 2H), 7.80–7.83 (m, 1H), 7.76–7.71 (m, 1H), 7.19–7.07 (m, 2H), 7.07–7.01 (m, 1H), 6.98–6.90 (m, 2H), 6.83 (app. t, J = 7.4 Hz, 1H), 6.31 (app. t, J = 7.7, 2H), 4.77 (s, 3H, $\mathbf{H_{Me}}$). ^{13}C NMR

(acetone-d_6, δ, ppm): 168.9, 168.3, 158.3, 153.0, 151.2, 150.6, 149.6, 145.9, 145.3, 145.1, 143.7, 141.0, 139.7, 139.5, 132.7, 132.4, 131.2, 130.5, 127.8, 125.8, 125.3, 124.4, 124.1, 123.7, 123.2, 120.7, 120.5, 38.2 ($\mathbf{C_{Me}}$). Two C signals 145.3 ppm are likely to be overlapped. Anal. calcd for $C_{29}H_{23}N_7F_6PIr$: C 43.18, H 2.87, N 12.15. Found: C 43.26, H 2.66, N 11.93. HRMS (m/z) calcd for $C_{29}H_{23}N_7{}^{193}Ir$ $[M]^+$: 662.1644. Found: 662.1636. Single crystals for X-ray diffraction were grown from a slowly evaporating acetone/water solution.

$[Ir(ppy)_2P2]PF_6$ (IrP2). Yield: 0.07 g (46%). ^{1}H NMR (acetone-d_6, δ, ppm): 8.60 (d, J = 7.9 Hz, 1H), 8.37 (app. t, J = 7.9 Hz, 1H), 8.26–8.21 (m, 2H), 8.08–8.01 (m, 2H), 8.01–7.93 (m, 2H), 7.91–7.75 (m, 4H), 7.18–7.10 (m, 2H), 7.08–7.02 (m, 1H), 7.01–6.96 (m, 1H), 6.89–6.95 (m, 1H), 6.88–6.82 (m, 1H), 6.35–6.30 (m, 2H), 4.56 (s, 3H, $\mathbf{H_{Me}}$). ^{13}C NMR (acetone-d_6, δ, ppm): 168.8, 168.2, 167.7, 152.1, 151.1, 150.5, 148.7, 145.7, 145.3, 145.2, 145.1, 141.5, 139.8, 139.7, 132.9, 132.3, 131.3, 130.6, 130.5, 125.9, 125.5, 125.4, 124.5, 124.4, 123.8, 123.3, 120.8, 120.6, 42.43 ($\mathbf{C_{Me}}$). Calcd for $C_{29}H_{23}N_7F_6PIr$: C 43.18, H 2.87, N 12.15. Found: C 42.51, H 2.78, N 11.68. HRMS (m/z) calcd for $C_{29}H_{23}N_7{}^{193}Ir$ $[M]^+$: 662.1644. Found: 662.1626. Single crystals for X-ray diffraction were grown from a slowly evaporating acetone/water solution.

$[Ir(ppy)_2Q1]PF_6$ (IrQ1). Yield: 0.02 g (31%). ^{1}H NMR (acetone-d_6, δ, ppm): 9.06 (d, J = 8.6 Hz, 1H), 8.91 (d, J = 8.7 Hz, 1H), 8.30 (d, J = 8.4 Hz, 1H), 8.27–8.20 (m, 2H), 8.16–8.11 (m, 1H), 8.00–7.94 (m, 2H), 7.93–7.80 (m, 4H), 7.76 (app. t, J = 7.5 Hz, 1H), 7.41–7.35 (m, 1H), 7.02–6.98 (m, 5H), 6.82 (app. t, J = 8.2 Hz, 1H), 6.45 (d, J = 8.4 Hz, 1H), 6.14 (d, J = 7.7 Hz, 1H), 4.86 (s, 3H, $\mathbf{H_{Me}}$). ^{13}C NMR (acetone-d_6, δ, ppm): 168.6, 167.9, 159.1, 151.8, 151.7, 150.3, 148.9, 145.2, 145.1, 144.3, 142.7, 141.5, 139.5, 139.4, 133.3, 132.4, 131.5, 131.1, 131.0, 130.9, 130.4, 129.9, 129.5, 125.9, 125.1, 124.2, 123.8, 123.3, 123.2, 122.1, 120.5, 120.4, 38.5 ($\mathbf{C_{Me}}$). Anal. calcd for $C_{33}H_{25}N_7F_6PIr$: C 46.26, H 2.94, N 11.44. Found: C 45.56, H 2.90, N 11.01. HRMS (m/z) calcd for $C_{22}H_{16}N_2{}^{193}Ir$ $[M\{\text{-}Q1\}]^+$: 501.0943. Found: 501.0933. Calcd for $C_{33}H_{25}N_7{}^{193}Ir$ $[M]^+$: 712.1801. Found: 712.1790. Single crystals for X-ray diffraction were grown from a slowly evaporating acetone/water solution.

$[Ir(ppy)_2Q2]PF_6$ (IrQ2). Yield: 0.07 g (83%). ^{1}H NMR (acetone-d_6, δ, ppm): 8.96 (d, J = 8.7 Hz, 1H), 8.65 (d, J = 8.4 Hz, 1H), 8.26 (d, J = 7.7 Hz, 1H), 8.20–8.10 (m, 3H), 8.08 (d, J = 6.5 Hz, 1H), 8.01–7.96 (m, 1H), 7.95–7.93 (m, 1H), 7.91–7.82 (m, 3H), 7.72–7.67 (m, 1H), 7.38–7.31 (m, 1H), 7.10–7.05 (m, 3H), 7.04–6.98 (m, 2H), 6.86–6.80 (m, 1H), 6.43 (d, J = 7.6 Hz, 1H), 6.17 (d, J = 7.7 Hz, 1H), 4.58 (s, 3H, $\mathbf{H_{Me}}$). ^{13}C NMR (acetone-d_6, δ, ppm): 168.6, 168.4, 167.9, 151.8, 150.6, 150.3, 148.7, 147.3, 145.1, 144.5, 143.0, 140.8, 139.6, 139.5, 132.9, 132.3, 131.7, 131.4, 131.1, 130.5, 130.2, 130.1, 128.8, 125.9, 125.2, 124.5, 124.0, 123.4, 123.3, 120.8, 120.6, 120.4, 42.3 ($\mathbf{C_{Me}}$). Anal. calcd for $C_{33}H_{25}N_7F_6PIr\cdot(CH_2Cl_2)$: C 43.36, H 2.89, N 10.41. Found: C 44.03, H 2.46, N 10.61. HRMS (m/z) calcd for $C_{22}H_{16}N_2{}^{193}Ir$ $[M\{\text{-}Q1\}]^+$: 501.0943. Found: 501.0933. Calcd for $C_{33}H_{25}N_7{}^{193}Ir$ $[M]^+$: 712.1801. Found: 712.1793. Single crystals for X-ray diffraction were grown by diffusion of hexanes into a dichloromethane solution.

X-ray crystallography

Crystal and refinement data is provided in the SI (Tables S1 and S2). All data was collected using an XtaLAB Synergy, single source at home/near HyPix diffractometer operating around T = 100 (10) K using Cu Kα (λ = 1.54184 Å) radiation. The diffraction pattern was indexed and the total number of runs and images was based on the strategy calculation from the program CrysAlisPro (Rigaku, V1.171.40.53, 2019). The unit cell was refined, and the data reduction, scaling, and absorption corrections were performed using CrysAlisPro (Rigaku, V1.171.40.53, 2019). The structures were solved and the space group determined by the ShelXT[20] structure solution program using Intrinsic Phasing and by using Olex2 [21] as the graphical interface. Refinement was done by Least Squares using version 2018/3 of ShelXL. All non-hydrogen atoms were refined anisotropically. Hydrogen atom positions were calculated geometrically and refined using the riding model. The solvent mask function of Olex2 was used for **IrQ2** to remove 0.375[CH_2Cl_2].

Photophysical measurements

Absorption spectra were measured on an Agilent Technologies Cary 4000 double-beam UV-Vis spectrophotometer and baseline corrected. Uncorrected excitation and emission spectra were recorded using an Edinburgh FLSP980-stm spectrophotometer equipped with a Xe arc lamp (450 W), double excitation and emission monochromators, and a Peltier-cooled Hamamatsu R928P photomultiplier. The spectra were corrected for source intensity (lamp and grating) and emission spectral response (detector and grating) by a calibration curve supplied with the instruments. Excited state lifetimes (τ) were determined by means of time-correlated single photon counting (TCSPC) with the same Edinburgh FLSP980-stm spectrometer, using pulsed picosecond LEDs (377 nm, FHWM < 800 ps) as the excitation source. The goodness of fit was assessed by minimising the reduced χ^2 function and by visual inspection of the weighted residuals. Photoluminescence quantum yields (Φ) in solution were obtained from the corrected spectra on a wavelength scale (nm) and measured according to the approach described by Demas and Crosby, using an air-equilibrated aqueous solution of tris(2,2′-bipyridyl)ruthenium(II) dichloride as reference (Φ_{ref} = 0.028).[22,23]

Density functional theory calculations

All density functional theory (DFT) calculations were performed using the ORCA 6.0 package using a long-range corrected hybrid exchange and correlation functional (CAM-B3LYP) with the triple-ζ basis set and Grimme's D4 van der Waals correction.[24–26] The CPMP implicit solvent method for dichloromethane was used to mimic the effects of the solvent. After the geometry optimisation of the complexes, the vibrational frequencies were calculated to ensure that a stable minimum was located, and the absorption spectra of the complexes were calculated using Time Dependent Density Functional Theory (TD-DFT)[27,28] with the Tamm–Dancoff approximation.[29] The energies of the HOMO and LUMO orbi-

tals were estimated by computing the ionisation energy and electron affinity of the complexes doing a single point calculations at the optimised geometry for the oxidised and reduced molecules, respectively.[30]

Cyclic voltammetry

All electrochemical measurements were performed in acetonitrile containing 0.1 M tetrabutylammonium hexafluorophosphate ($TBAPF_6$) and the rhenium or iridium complex at concentration of *ca.* 2 mM. The measurements were performed using a CH Instruments 910B, coupled to a three-electrode electrochemical cell containing a leakless Ag/AgCl reference electrode (ET072-1 model, EDAQ), a platinum wire counter electrode (Goodfellow) and 1 mm glassy carbon working electrodes (ET074-1 model, EDAQ). Prior to experiments, the acetonitrile solutions were degassed by bubbling nitrogen to remove oxygen. During the electrochemical experiments, a stream of nitrogen was blown over the surface of the solution to maintain a deoxygenated environment.

Imaging

Mouse brain tissue used in this study were from C57Bl6/J mice and were excess to the needs of other experiments. All animal work was approved by the Curtin University animal ethics committee (ARE2023-3) and conducted according to the Australian code for the care and use of animals for scientific purposes.[31] Mice were humanely sacrificed under isoflurane anaesthesia by cervical dislocation; brain tissue was obtained quickly, and flash frozen in liquid nitrogen-cooled isopentane. Coronal tissues of the cerebellum (10 μm thick) were cut on a cryotome Leica CM1520 at −18 °C and melted onto glass microscopy slides. The samples were then allowed to air dry at room temperature prior to fixation with paraformaldehyde [4% in phosphate-buffered saline (PBS)] for 10 minutes. Slides were then washed with PBS for 10 minutes and stained *via* 60 min incubation at room temperature with the probe solution [20 μM solution of metal complex in 0.2% DMSO in tris-buffered saline (TBS), 900 μL per tissue section]. The probe solution was prepared by dissolving the complexes in pure DMSO, followed by immediate dilution with PBS. Excess probe solution was washed off with deionized water followed by rinsing with PBS for 10 minutes three times. Slides were then allowed to dry at room temperature prior to imaging. Mounting media with DAPI was used. Blank experiments were prepared from native tissues, treated with all reagents, except incubation in metal complex solution. Fluorescence microscopy imaging was performed on a Nikon A1+ confocal microscope with NIS Elements software. Laser excitation at 402 nm was used with 20/80 dichroic mirror to allow collection of all emission wavelengths. The spectral detector collected at 10 nm bands from 504 nm to 724 nm with a pinhole radius of 12.77 using a 10× objective (NA = 0.45) and 20× objective (NA = 0.75). Fluorescence microscopy imaging was performed on a Nikon Ti2-U inverted microscope with a DS-Q12 camera, pE-300 white LED fluorescence lamp, and NIS Elements standard software. Images were gathered at an exposure time of 600 ms and an analog gain of 7.6%. Images were adjusted for brightness, contrast and a scale bar was added using ImageJ.[32] To confirm stain localization to lipid rich myelin in brain white matter tracts, correlative optical microscopy and Fourier transform infrared (FTIR) microscopy was performed. Optical microscopy was performed as described above, using stained tissues on glass slides, which have an infrared transparent window across the lipid C–H stretching region (~2800–3050 cm^{-1}). FTIR microscopy images were collected with a Nicolet iN 10MX FTIR microscope, equipped with an 8 × 2 pixel liquid nitrogen cooled linear array detector and 25 μm pixel size. Spectra were collected at 8 cm^{-1} spectral resolution with 4 coadded scans, with data collected in transmission geometry.

Lipophilicity

The values of $\log D_{7.4}$ for the Ir(III) complexes were measured with the shake-flask method using PBS and *n*-octanol, following a previously published procedure.[33]

Results and discussion

Synthesis and characterisation

Methylation of 2-(1*H*-tetrazol-5-yl)pyridine and 2-(1*H*-tetrazol-5-yl)quinoline was performed by reaction with CH_3I in acetone at 100 °C within a pressurised vessel, which yielded both the corresponding *N*1 and *N*2-methylated regioisomers. Both pairs of isomers, 2-(1-methyl-1*H*-tetrazol-5-yl)pyridine (**P1**) and 2-(2-methyl-2*H*-tetrazol-5-yl)quinoline (**P2**) or 2-(1-methyl-1*H*-tetrazol-5-yl)quinoline (**Q1**) and 2-(2-methyl-2*H*-tetrazol-5-yl)quinoline (**Q2**), could be easily separated by flash chromatography. The ^{13}C NMR spectra of these ligands display diagnostic peaks for the tetrazolic *ipso* C atom (Fig. S3, S7, S11 and S15), with values greater and lower than 160 ppm for *N*2 and *N*1-methylation, respectively.[34] The corresponding Re(I) complexes **ReP1–2** and **ReQ1–2** (Fig. 1) were prepared by reaction of equimolar amounts of $[ReBr(CO)_5]$ and tetrazole ligand in toluene. At the end of the reaction, the targeted complexes could be isolated in good to high yield by simple filtration and washing. On the other hand, the Ir(III) complexes **IrP1–2** and **IrQ1–2** (Fig. 1) were prepared in good to high yield by reacting the dimer $[Ir(\mathbf{ppy})(\mu\text{-}Cl)]_2$ with a slight excess of tetrazole ligand in a mixture of CH_2Cl_2 and EtOH at room temperature, followed by precipitation *via* anion exchange (PF_6^- for Cl^-). The structures of the eight metal complexes were confirmed by ^1H and ^{13}C NMR spectroscopy (Fig. S2–S45), elemental analysis, single crystal X-ray diffraction and high-resolution mass spectrometry (Fig. S46–S53). The complexes **IrP2**[35] and **IrQ2**[16] were previously published by direct methylation of the corresponding neutral complexes, with the obtained data matching those reported in the literature. In general, the chemical shift values for the signals corresponding to the H atoms of the ligands display a slight deshielding effect upon coordination, which is particularly evident in the case of the Re(I) complexes as the number of signals is the same between the free ligands and the complexes. Furthermore, the signal corresponding to the

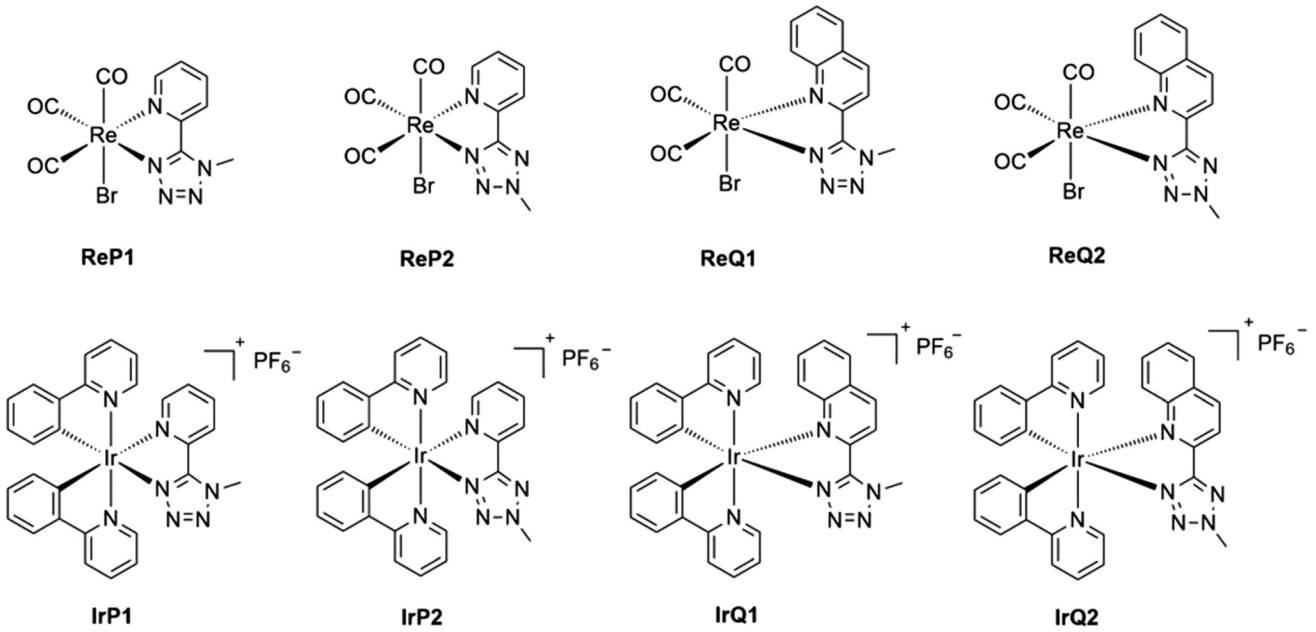

Fig. 1 Structures of the synthesised Re(I) and Ir(III) complexes.

H4 atom of the quinoline moiety appears more deshielded than the signal of H9 (see Fig. S1 for numbering scheme), but this order is inverted upon complexation with Re(I) for both **ReQ1** and **ReQ2**. The IR spectra of the Re(I) complexes (Fig. S54–S57) display the expected strong signals corresponding to the stretching modes of the CO ligands in *facial* configuration in the 2100–1900 cm^{-1} region, with values typical for complexes of neutral charge.[36,37] The HRMS spectra of the Re(I) complexes coordinated to the pyridyl-tetrazole ligand consistently display the debrominated fragment $[Re(CO)_3(\mathbf{NN})]^+$ and the solvato-complex $[Re(CO)_3(\mathbf{NN})(NCCH_3)]^+$ (**NN** = diimine-bound methylated pyridyl or quinolyl tetrazole). Conversely, the Re(I) complexes bound to the quinolyl ligands display the solvato-complex $[Re(CO)_3(\mathbf{NN})(NCCH_3)]^+$. All the Re-containing fragments display the typical isotopic distribution of the metal centre. The molecular ion of the Ir(III) complexes is visible for **IrP1** and **IrP2**, along with the fragments obtained by decomplexation of the tetrazole ligands. The latter are the main peaks observed for the Ir(III) complexes **IrQ1** and **IrQ2** bound to the quinoline ligand. As in the case of Re(I), these peaks match the isotopic distribution of Ir.

X-ray crystal structures

Single crystals were obtained for all the prepared complexes (Fig. 2, with selected crystallographic data available in Tables S1 and S2). All complexes were monoclinic in the space group $P2_1/c$ except for **ReP2** and **ReQ2**, which were triclinic ($P\bar{1}$). Each complex possessed slightly distorted octahedral geometries. The structures of the Re(I) complexes display the expected *facial* configuration of the three CO ligands. On the other hand, the Ir(III) complexes reveal a *trans* arrangement of the two pyridine rings of the cyclometalated **ppy** ligands. In all cases, the complexes containing the *N*2-methylated ligands direct the methyl substituent in *anti* orientation with respect to the metal centre, as the analogous *syn* complex would presumably be too sterically hindered. The tetrazole and pyridine ligands are quasi-coplanar, exhibiting a torsion angle around 2–4° for the *N*2-methylated ligands, and 7–8° for the *N*2-methylated analogues. On the other hand, the torsion is slightly enhanced for the quinoline ligands, increasing to 11–17°. In terms of bond lengths, there does not appear to be any significant difference in the metal–nitrogen bonds when comparing the *N*1 and *N*2-methylated pairs, indicating a similar bond strength.

Photophysical properties

A summary of the photophysical data for the synthesised complexes is presented in Table 1. The combined absorption spectra are shown in Fig. 3. Overall, the spectra are analogous and display intense high energy bands associated to ligand centred (LC) $\pi\pi^*$ transitions at wavelengths shorter than 350 nm, followed by bands of lower intensity ascribed to metal-to-ligand charge transfer (MLCT) transitions, with partial admixture of ligand-to-ligand charge transfer (LLCT) transitions.[36] For the Ir(III) complexes, the broad CT band is likely to be composed of spin-allowed singlet-to-singlet as well as spin-forbidden singlet-to-triplet transitions, with the latter occurring at lower energies.[38]

To confirm the nature of the electronic transitions observed in the absorption spectra TD-DFT calculations were performed. Fig. 4 shows the frontier HOMOs and LUMOs involved in the most probable lower-energy transition for each complex

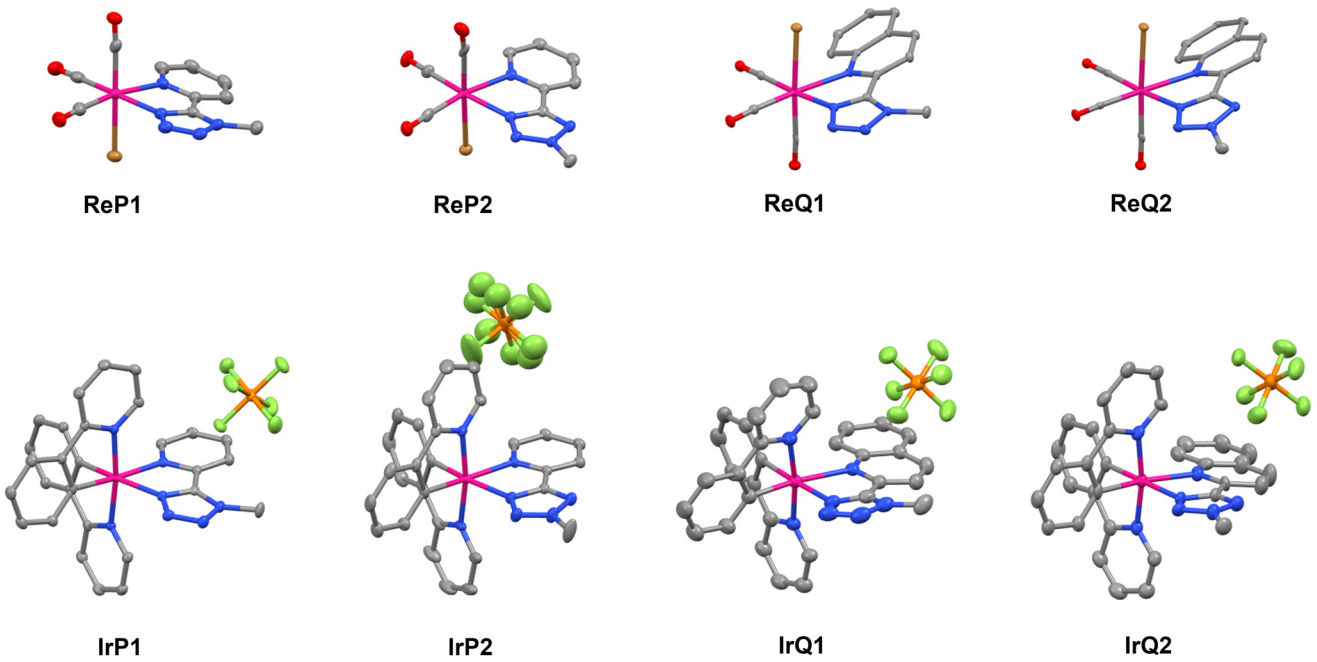

Fig. 2 X-ray crystal structures of the synthesised complexes. Hydrogen atoms are omitted for clarity.

Table 1 Summary of the photophysical data for the synthesised complexes, measured from diluted (*ca.* 10^{-5} M) CH_2Cl_2 solutions

	λ_{abs} [nm] (ε [10^5 M^{-1} cm^{-1}])	λ_{em} [nm]	τ^a [ns]	$\Phi^{a,b}$ (%)
ReP1	230 (0.21), 272 (0.11), 400 (0.03) TD-DFT: 235, 252, 340	650	38	0.4[c]
ReP2	230 (0.13), 263 (0.07), 360 (0.02) TD-DFT: 238, 250, 318	580	480	2.8
ReQ1	261 (0.16), 328 (0.04), 430 (0.02) TD-DFT: 230, 282, 367	750	12	[d]
ReQ2	256 (0.28), 320 (0.05), 393 (0.02) TD-DFT: 225, 278, 341	680	201	0.5[c]
IrP1	268 (0.20), 310 (0.05), 380 (0.03) TD-DFT: 265, 300, 324	640	77	1.5[c]
IrP2 [e]	265 (0.18), 310 (0.06), 382 (0.02) TD-DFT: 268, 280, 323	560	516	24
IrQ1	261(0.30), 323 (0.09), 385 (0.05) TD-DFT: 276, 321, 325	715	29	[d]
IrQ2 [f]	256 (0.39), 310 (0.11), 375 (0.05) TD-DFT: 268, 303, 322	635	645	4.3

TD-DFT absorption maxima are reported along with experimental values. The absorption wavelengths obtained from TD-DFT calculations are indicative of trends only, as exact quantitative agreement is unexpected. Nevertheless, they display a consistent trend with the experiments. [a] Measured from degassed solutions. [b] Measured against a tris(2,2′-bipyridyl)ruthenium(II)dichloride aqueous solution, used as reference (Φ = 2.8%).[23] [c] The values are slightly underestimated due to the spectral range of the detector. [d] The value cannot be accurately determined due to the spectral range of the detector. [e] Data previously reported.[35] [f] Data previously reported.[16]

(Fig. S58–S65). For the Re(I) complexes, the HOMOs are mainly composed of the metal 5d orbitals, with involvement of the orbitals of the CO and Br ligands of π symmetry. The LUMOs are mainly localised on the π*-conjugated system of the tetrazolyl pyridine or quinoline ligand. Similarly, the HOMOs in the Ir(III) complexes involve the metal 5d orbitals and the π system of the **ppy** ligands, whereas the LUMOs extend over the tetrazolyl pyridine or quinoline ligand. The calculations suggest that the position of the methyl substituent on the tetrazole ring has a more profound influence on the energy of the LUMOs, consistently for all the complexes. *N*1-Methylation results in a stabilisation of the energy of the LUMO relative to the *N*2-methylation. On the other hand, the energy of the HOMO orbital remains relatively unaffected.

Excitation of the complexes at 370 nm to their MLCT excited state manifolds reveals in all cases visible emission in diluted CH_2Cl_2 solution at room temperature. The emission bands are broad and structureless, as typical of radiative decay from excited states of CT nature (Fig. 5).[36] The corresponding excitation spectra display peaks that are consistent with the previously shown absorption spectra (Fig. S66–S73). The emission maxima appear to be significantly affected by both the aromatic substituent on the tetrazole ring and the position of the methyl substituent (*e.g.* *N*1 or *N*2). Considering the same methylated regioisomer, the substitution of the pyridine for the quinoline ring favours a bathochromic shift of the emission band (100 and 75 nm for Re(I) and Ir(III), respectively). This trend is expected by the increased conjugation stabilising the π* orbitals and lowering the relative energy of the excited state. On the other hand, when comparing complexes bearing the same pyridine or quinoline substituent, methylation of the *N*1 position of the tetrazole ring results in a bathochromic shift of the emission band (70 and 80 nm for Re(I) and Ir(III), respectively). This trend agrees with the TD-DFT data indicating that methylation of the N1 atom increases the stabilisation

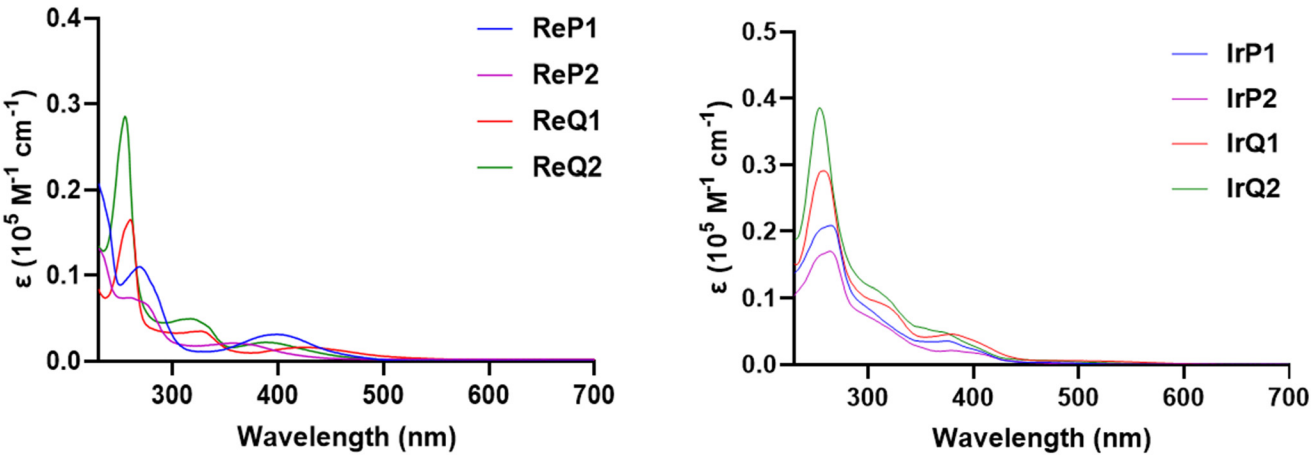

Fig. 3 Absorption spectra of the synthesised complexes measured from diluted (*ca.* 10^{-5} M) CH_2Cl_2 solutions.

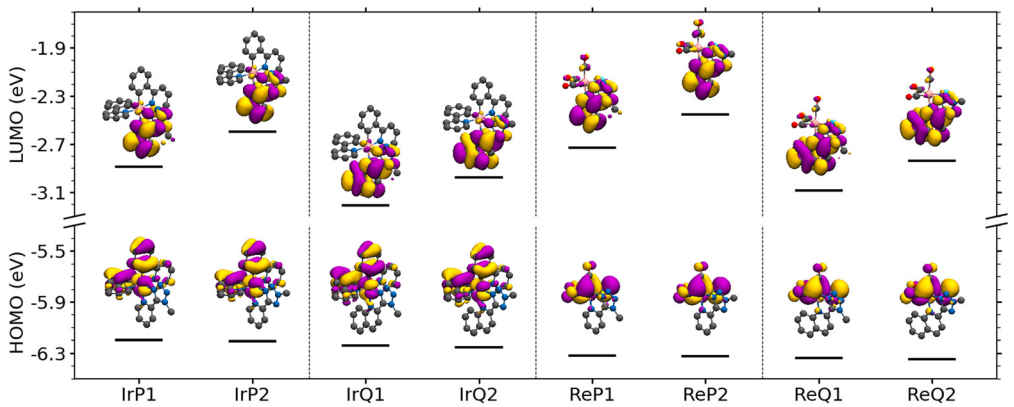

Fig. 4 Molecular orbital renderings for the HOMOs and LUMOs of each complex using an isovalue of 0.025. In each case, the HOMO to LUMO transition represents the lowest energy excitation.

of the π-system of the pyridine and quinoline substituents. This effect is particularly evident when considering that the redshifted emission band of **ReP1** overlaps with that of **ReQ2**, and the same occurs for the corresponding **IrP1** and **IrQ2** complexes. A similar trend was previously reported for Cu(I) complexes by Bryce and co-workers.[19]

The complexes display monoexponential and relatively long-lived excited states (Table 1), as typical of spin-forbidden phosphorescent emission from ^{3}MLCT excited states (Fig. S74–S81). Consistently, the excited state lifetimes τ are shortened in aerated solutions, supporting emission from excited states of triplet multiplicity. A similar trend is observed for the values of photoluminescent quantum yields, although these values could only be underestimated for some of the complexes given that part of the emission band is not recorded due to the detector spectral range. The values of τ correlate with the maximum of the emission, whereby the redshifted *N*1-methylated complexes in each pair display shorter excited state decays. This trend is associated with the energy gap law,[39] meaning that non-radiative decay constants are enhanced as the energy gap between the excited and ground states reduces.

Electrochemical properties

To further validate the conclusion that the lower energy of the excited state for the *N*1 regioisomer is predominantly caused by a stabilisation of the π* orbitals of the tetrazole ligand, the Re(I) and Ir(III) were investigated by means of cyclic voltammetry. The measured voltammograms, reported from acetonitrile solutions using $[NBut_4][PF_6]$ as supporting electrolyte against a Ag/AgCl reference electrode, are shown in Fig. S82, with a summary of calculated oxidation and reduction potential values shown in Table 2. At positive potentials, the Re(I) complexes display rather irreversible one-electron processes in the range 1.55–1.63 V. On the other hand, at negative potentials, the first reduction process occurs in a reversible manner (aside from **ReP2**), with the reduction potential of **ReP1** and **ReQ1** being systematically at higher values (−1.22 and −0.91 V, respectively) with respect to **ReP2** and **ReQ2** (−1.38 and −1.09 V, respectively). Similarly, the Ir(III) complexes display reversible one-electron oxidation processes in the range 1.41–1.45 V. Their reduction potentials follow the same trend as the Re(I) complexes, with higher values for **IrP1** and **IrQ1** (−1.27 and

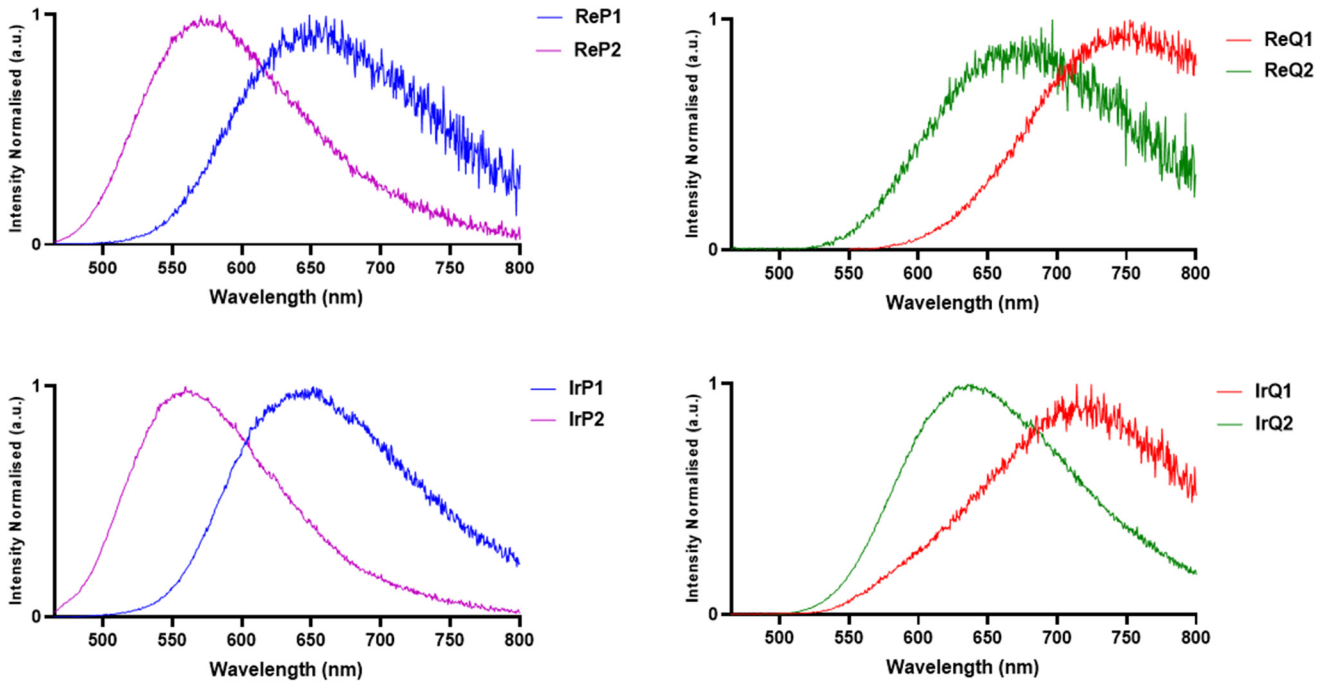

Fig. 5 Emission spectra of the synthesised complexes measured from diluted (*ca.* 10^{-5} M) CH_2Cl_2 solutions (λ_{exc} = 370 nm).

Table 2 Summary of the main cyclic voltammetry data obtained from 2.0 mM acetonitrile solutions, using $[NBut_4][PF_6]$ (0.1 M) as support electrolyte; half-wave potentials (for reversible processes) are reported relative to the Ag/AgCl reference electrode

	E_{ox} [V]	E_{red} [V]
ReP1	1.55[a]	−1.22
ReP2	1.54[a]	−1.38
ReQ1	1.57[a]	−0.91
ReQ2	1.63[a]	−1.09
IrP1	1.41	−1.27
IrP2	1.40	−1.49
IrQ1	1.46	−0.92
IrQ2	1.45	−1.16

[a] Irreversible process.

−0.92 V, respectively) with respect to **IrP2** and **IrQ2** (−1.49 and −1.16, respectively). Furthermore, and as expected, the complexes bearing the quinoline substituent are more easily reduced with respect to the analogous complex bound to the pyridine-containing ligand, because of the stabilisation of the π* system due to extended conjugation.

Brain tissue staining

The synthesised Re(I) and Ir(III) complexes were evaluated as luminescent probes for staining mouse brain and cerebellum tissue with confocal and epifluorescence microscopy. The Re(I) complexes did not exhibit significant staining capability, yielding images often indistinguishable from the unstained control samples (data not shown). The complexes **IrP1** and **IrP2** produced images with bright particulates across all tissue sections, suggesting lack of staining due to extensive precipitation in the medium. In contrast, the **IrQ1** and **IrQ2** complexes demonstrated clear staining in both brain and cerebellum sections (Fig. 6 and 7). To ensure the stability of the Ir(III) complexes in biological medium, their absorbance spectra were recorded at time intervals for a period of 48 hours. The spectra were recorded in pure DMSO and PBS containing 1% DMSO to obtain a direct comparison with the preparation of the solutions for the staining experiments. The recorded spectra are shown in Fig. S83 and S84. The complexes **IrQ1** and **IrQ2** appear to undergo decomposition in pure DMSO, which is ascribed to the dissociation of the tetrazole ligand. The corresponding **IrP1** and **IrP2** appear stable. On the other hand, no change in the spectra is observed from the complexes in PBS solution with 1% DMSO. These data suggest that the Ir(III) complexes cannot be stored in the stock DMSO solution, but must be immediately diluted with PBS. The photoluminescence quantum yields of the Ir(III) complexes were also recorded in aerated PBS solution, displaying significantly reduced values when compared to those reported from degassed dichloromethane solutions (Table 1), as expected. The measured values range between 0.01 and 0.11% [**IrP1** (0.08%), **IrP2** (0.35%), **IrQ1** (0.01%), **IrQ2** (0.11%)]. These values might appear as a drawback. However, it should be noted that once the complexes are incubated within the lipophilic regions of the tissue, their environment is likely to be significantly different from the aqueous environment from the PBS solutions.

Images were acquired using a confocal microscope with an excitation wavelength of 402 nm, and emission was recorded between 500 and 600 nm using a spectral detector. Fig. 6 shows the staining of the Ir(III) complexes in brain tissue sections, highlighting the ability of the complexes to stain lipid-

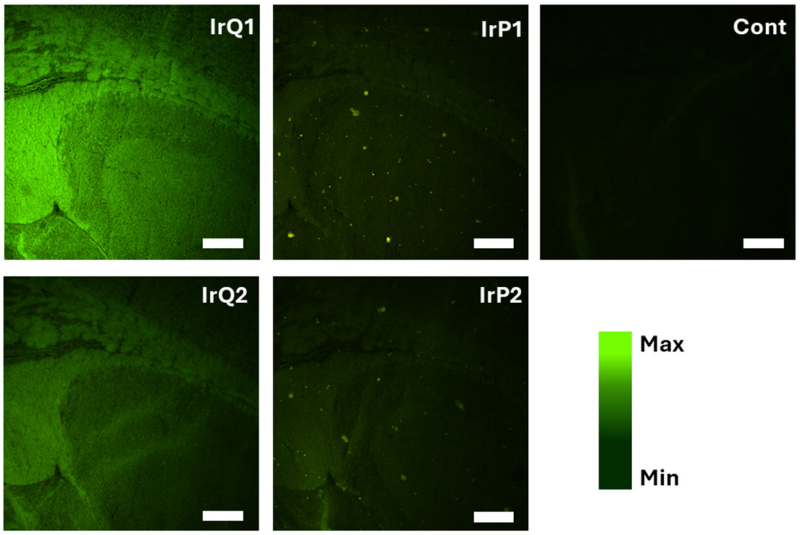

Fig. 6 Confocal brain images of brain tissue stained with the Ir(III) complexes. Scale bar = 200 μm.

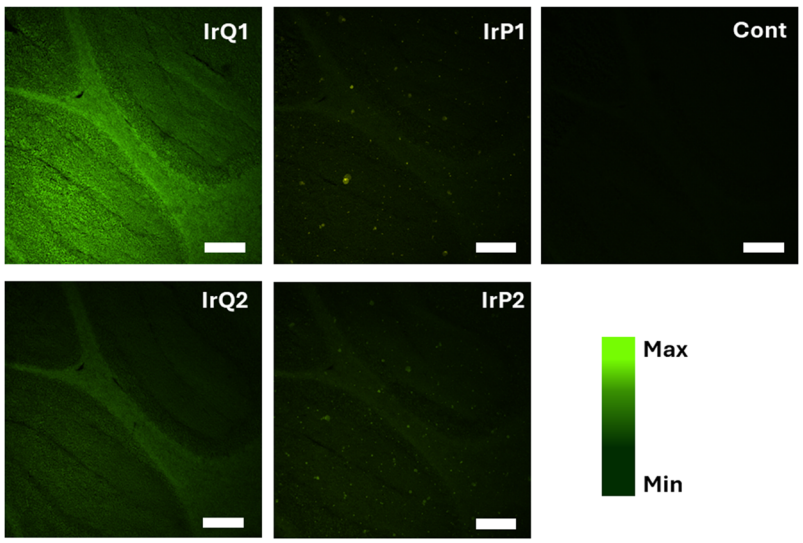

Fig. 7 Confocal brain images of cerebellum tissue stained with the Ir(III) complexes. Scale bar = 200 μm.

rich myelinated regions of the corpus callosum white matter tracts. In a similar fashion, in the cerebellum tissue (Fig. 7), the complexes show a marked affinity for the inner white matter layer, which is comprised of lipid-rich myelin. To confirm the preferential affinity for lipid-rich myelin, a correlative FTIR microscopy and fluorescence microscopy experiment was undertaken (Fig. 8). Using the $\nu_s(CH_2)$ absorbance band of lipid acyl chains as a marker of lipid content, correlative FTIR and fluorescence microscopy on the same sample clearly highlight the localisation of **IrQ1** to lipid-rich myelin within the inner white matter layers of the cerebellum (Fig. 8). Between **IrQ1** and **IrQ2**, **IrQ1** displayed higher luminescence intensity in both brain and cerebellum tissues than **IrQ2**. Brain and cerebellum tissues stained with the Ir(III) complexes could also be imaged on a more accessible and cost-effective epifluorescence microscope using a FITC filter set. The results were consistent with those obtained by confocal microscopy, confirming similar staining patterns (Fig. S85 and S86).

At this stage the exact lipid targets of the probes remain unknown, and it is possible that the staining pattern represents ubiquitous lipophilicity. Comparing their lipophilicity through their measured $\log D_{7.4}$ values, the *N*2-methylated complexes appear to be systematically more lipophilic than the corresponding *N*1 complexes (Table S3). However, without currently knowing the lipid targets of these complexes, and considering that the current experiments are performed on tissue rather than cells, it is not straightforward to generalise a trend between the staining capacity and the lipophilicity of the individual complexes. The results highlight the current potential of these probes to be used to study myelin formation in

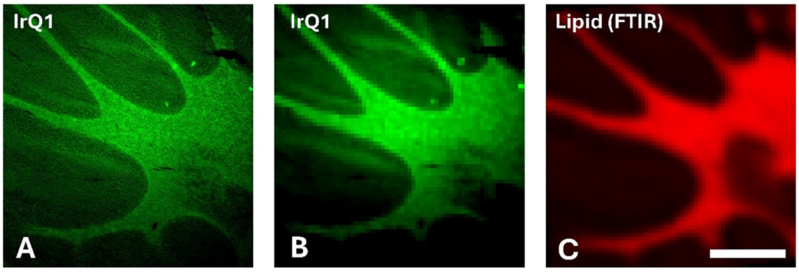

Fig. 8 Correlative fluorescence microscopy and FTIR microscopy confirm **IrQ1** staining is in lipid-rich myelinated white matter tracts. (A) Fluorescence image of **IrQ1**, (B) same image as panel A, binned to match pixel size (25 μm) of FTIR microscopy, (C) FTIR microscopy of lipid distribution, using $\nu_s(CH_2)$ of acyl chains as a spectroscopic lipid marker. Scale bar = 500 μm.

brain tissue, or demyelination during disease such as multiple sclerosis, Alzheimer's disease or following brain trauma. Further, these current probes now serve as a starting point for further photophysical tuning to enable multiplexing,[40] additional correlative microscopy (*e.g.*, correlative optical and X-ray fluorescence),[41] or ligand modification to confer increased molecular specificity to classes of lipids.

Conclusions

*N*1 and *N*2 methylated regioisomers of 2-pyridyl and 2-quinolyl tetrazoles have been bound to Re(I) tricarbonyl and cyclometalated Ir(III) complexes, obtaining a small family of luminescent complexes. The photophysical investigation suggests that these complexes emit from ^{3}MLCT excited states. The photophysical properties of these complexes highlight the significant effect of the regiomethylation, indicating that methylation of the N1 atom of the tetrazole ring results in a stronger stabilisation of the π-conjugated system of the pyridyl and quinolyl substituent. This effect is consistently evidenced by redshifted absorption and emission bands, as well as the lower reduction potential for the complexes bound to the *N*1-methylated ligand. TD-DFT calculations support the notion that methylation of the N1 atom has a stabilising effect on the energy of the LUMO, while leaving the energy of the HOMO relatively unaffected. Among the synthesised complexes, **IrQ1** and **IrQ2** have displayed strong potential as stains for lipid-rich regions of both brain and cerebellum tissues. While the staining pattern of these two complexes is very similar, a consistently stronger signal is detected from **IrQ1** by means of epifluorescence and confocal microscopy. This work suggests that regiomethylation of tetrazole ligands could serve to alter the photophysical properties of metal complexes while maintaining their localisation when used as probes for optical imaging of tissue.

Author contributions

Massi M. and Stagni S. designed and supervised the synthesis, characterisation and photophysical measurements. Hackett M. designed and supervised the staining experiments. Raiteri P. supervised the TD-DFT calculations. Moggach S. supervised the X-ray data analysis. Dallerba E. performed the synthesis, characterisation, photophysical investigation and staining of brain tissue, in conjunction with Ellison G. and Nesbit M. for the imaging. O'Conghaile P. performed the electrochemistry experiments. Cameron L. completed the X-ray data acquisition and refinement. Blake A. and Pearson E. performed the TD-DFT calculations. Turner E., Innes E., Strickling G. and Pangiarella J. completed various aspects of this work as undergraduate project students at Curtin University. All authors contributed to discussion and final writing of the manuscript.

Conflicts of interest

The authors have no conflict of interest to declare.

Data availability

Supplementary information (SI) is available. See DOI: https://doi.org/10.1039/d5dt01745a.

CCDC 2222555–2222562 contain the supplementary crystallographic data for this paper.[42a–h]

Acknowledgements

Confocal microscopy analysis was performed using the Curtin Health Innovation Research Institute Microscopy and Histology Shared Resources Laboratory. MJH gratefully acknowledges funding support from the Australian Research Council (ARC Discovery Grant DP220103091 and ARC Future Fellowship FT190100017). MJH, GE and BL gratefully acknowledge funding support from MS Australia (incubator grant, 23-IGR2-0261). ED and BL gratefully acknowledge funding support from an AINSE Early Career Researcher Grant (AINSE-ECRG). BIA thanks the Australian Research Council for funding through grant FL180100087. Ryan J. Morris (Curtin University) is acknowledged for useful discussion. This work was supported by resources provided by the Pawsey

Supercomputing Research Centre with funding from the Australian Government and the Government of Western Australia, as well as by the National Computational Infrastructure through an NCMAS allocation.

References

1 V. V. G. K. Inavalli, V. Puente Muñoz, J. E. Draffin and J. Tønnesen, *Front. Cell. Neurosci.*, 2024, **18**, 1330100.
2 K. Kikuchi, L. D. Adair, J. Lin, E. J. New and A. Kaur, *Angew. Chem., Int. Ed.*, 2023, **62**, e202204745.
3 B. J. Schwehr, D. Hartnell, G. Ellison, M. T. Hindes, B. Milford, E. Dallerba, S. M. Hickey, F. M. Pfeffer, D. A. Brooks, M. Massi and M. J. Hackett, *Analyst*, 2024, **149**, 4536–4552.
4 G. Jiang, H. Liu, H. Liu, G. Ke, T.-B. Ren, B. Xiong, X.-B. Zhang and L. Yuan, *Angew. Chem.*, 2024, **136**, e202315217.
5 C. Eggeling, A. Volkmer and C. A. M. Seidel, *ChemPhysChem*, 2005, **6**, 791–804.
6 Y. W. Jun, H. R. Kim, Y. J. Reo, M. Dai and K. H. Ahn, *Chem. Sci.*, 2017, **8**, 7696–7704.
7 S. Barysaitė, J. Chmeliov, L. Valkunas and A. Gelzinis, *J. Phys. Chem. B*, 2024, **128**, 4887–4897.
8 L. C.-C. Lee and K. K.-W. Lo, *Chem. Rev.*, 2024, **124**, 8825–9014.
9 J. Twilton, C. Le, P. Zhang, M. H. Shaw, R. W. Evans and D. W. C. MacMillan, *Nat. Rev. Chem.*, 2017, **1**, 0052.
10 C. Bizzarri, E. Spuling, D. M. Knoll, D. Volz and S. Bräse, *Coord. Chem. Rev.*, 2018, **373**, 49–82.
11 V. Fernández-Moreira, F. L. Thorp-Greenwood and M. P. Coogan, *Chem. Commun.*, 2010, **46**, 186–202.
12 V. W.-W. Yam and A. S.-Y. Law, *Coord. Chem. Rev.*, 2020, **414**, 213298.
13 G.-X. Xu, E. C.-L. Mak and K. K.-W. Lo, *Inorg. Chem. Front.*, 2021, **8**, 4553–4579.
14 K. K.-W. Lo, *Acc. Chem. Res.*, 2020, **53**, 32–44.
15 C. A. Bader, E. A. Carter, A. Safitri, P. V. Simpson, P. Wright, S. Stagni, M. Massi, P. A. Lay, D. A. Brooks and S. E. Plush, *Mol. BioSyst.*, 2016, **12**, 2064–2068.
16 C. Caporale, C. A. Bader, A. Sorvina, K. D. M. MaGee, B. W. Skelton, T. A. Gillam, P. J. Wright, P. Raiteri, S. Stagni, J. L. Morrison, S. E. Plush, D. A. Brooks and M. Massi, *Chem. – Eur. J.*, 2017, **23**, 15666–15679.
17 M. V. Werrett, G. S. Huff, S. Muzzioli, V. Fiorini, S. Zacchini, B. W. Skelton, A. Maggiore, J. M. Malicka, M. Cocchi, K. C. Gordon, S. Stagni and M. Massi, *Dalton Trans.*, 2015, **44**, 8379–8393.
18 A. Sorvina, C. A. Bader, J. R. T. Darby, M. C. Lock, J. Y. Soo, I. R. D. Johnson, C. Caporale, N. H. Voelcker, S. Stagni, M. Massi, J. L. Morrison, S. E. Plush and D. A. Brooks, *Sci. Rep.*, 2018, **8**, 8191.
19 G. Li, R. S. Nobuyasu, B. Zhang, Y. Geng, B. Yao, Z. Xie, D. Zhu, G. Shan, W. Che, L. Yan, Z. Su, F. B. Dias and M. R. Bryce, *Chem. – Eur. J.*, 2017, **23**, 11761–11766.
20 G. M. Sheldrick, *Acta Crystallogr., Sect. C*, 2015, **71**, 3–8.
21 O. V. Dolomanov, L. J. Bourhis, R. J. Gildea, J. a. K. Howard and H. Puschmann, *J. Appl. Crystallogr.*, 2009, **42**, 339–341.
22 G. A. Crosby and J. N. Demas, *J. Phys. Chem.*, 1971, **75**, 991–1024.
23 K. Nakamaru, *Bull. Chem. Soc. Jpn.*, 1982, **55**, 2697–2705.
24 F. Neese, *Wiley Interdiscip. Rev.: Comput. Mol. Sci.*, 2022, **12**, e1606.
25 T. Yanai, D. P. Tew and N. C. Handy, *Chem. Phys. Lett.*, 2004, **393**, 51–57.
26 E. Caldeweyher, J.-M. Mewes, S. Ehlert and S. Grimme, *Phys. Chem. Chem. Phys.*, 2020, **22**, 8499–8512.
27 F. Neese and G. Olbrich, *Chem. Phys. Lett.*, 2002, **362**, 170–178.
28 M. Garcia-Ratés and F. Neese, *J. Comput. Chem.*, 2020, **41**, 922–939.
29 S. Hirata and M. Head-Gordon, *Chem. Phys. Lett.*, 1999, **314**, 291–299.
30 C.-G. Zhan, J. A. Nichols and D. A. Dixon, *J. Phys. Chem. A*, 2003, **107**, 4184–4195.
31 NHMRC, *Australian Code for the Care and Use of Animals for Scientific Purposes*, National Health and Medical Research Council, 8th edn, 2013.
32 J. Schindelin, I. Arganda-Carreras, E. Frise, V. Kaynig, M. Longair, T. Pietzsch, S. Preibisch, C. Rueden, S. Saalfeld, B. Schmid, J.-Y. Tinevez, D. J. White, V. Hartenstein, K. Eliceiri, P. Tomancak and A. Cardona, *Nat. Methods*, 2012, **9**, 676–682.
33 Y. W. Low, F. Blasco and P. Vachaspati, *Eur. J. Pharm. Sci.*, 2016, **92**, 110–116.
34 R. N. Butler and V. C. Garvin, *J. Chem. Soc., Perkin Trans. 1*, 1981, 390–393.
35 S. Stagni, S. Colella, A. Palazzi, G. Valenti, S. Zacchini, F. Paolucci, M. Marcaccio, R. Q. Albuquerque and L. De Cola, *Inorg. Chem.*, 2008, **47**, 10509–10521.
36 R. A. Kirgan, B. P. Sullivan and D. P. Rillema, in *Photochemistry and Photophysics of Coordination Compounds II*, ed. V. Balzani and S. Campagna, Springer, Berlin, Heidelberg, 2007, pp. 45–100.
37 A. M. Blanco-Rodríguez, M. Towrie, J.-P. Collin, S. Záliš and A. Vlček Jr., *Dalton Trans.*, 2009, 3941–3949.
38 F. Monti, A. Baschieri, L. Sambri and N. Armaroli, *Acc. Chem. Res.*, 2021, **54**, 1492–1505.
39 S. J. Jang, *J. Chem. Phys.*, 2021, **155**, 164106.
40 C. Andreou, R. Weissleder and M. F. Kircher, *Nat. Biomed. Eng.*, 2022, **6**, 527–540.
41 M. E. Graziotto, C. J. Kidman, L. D. Adair, S. A. James, H. H. Harris and E. J. New, *Chem. Soc. Rev.*, 2023, **52**, 8295–8318.
42 (*a*) CCDC 2222555: Experimental Crystal Structure Determination, 2025, DOI: 10.5517/ccdc.csd.cc2dlrb3; (*b*) CCDC 2222556: Experimental Crystal Structure Determination, 2025, DOI: 10.5517/ccdc.csd.cc2dlrc4; (*c*) CCDC 2222557: Experimental Crystal Structure Determination, 2025, DOI: 10.5517/ccdc.csd.cc2dlrd5;

(*d*) CCDC 2222558: Experimental Crystal Structure Determination, 2025, DOI: 10.5517/ccdc.csd.cc2dlrf6; (*e*) CCDC 2222559: Experimental Crystal Structure Determination, 2025, DOI: 10.5517/ccdc.csd.cc2dlrg7; (*f*) CCDC 2222560: Experimental Crystal Structure Determination, 2025, DOI: 10.5517/ccdc.csd.cc2dlrh8; (*g*) CCDC 2222561: Experimental Crystal Structure Determination, 2025, DOI: 10.5517/ccdc.csd.cc2dlrj9; (*h*) CCDC 2222562: Experimental Crystal Structure Determination, 2025, DOI: 10.5517/ccdc.csd.cc2dlrkb.